Size, Shape, and Charge of Salt-Free Catanionic Microemulsion Droplets: A Small-Angle Neutron Scattering and Modeling Study

4 AUTHORS, INCLUDING:

Bruno F B Silva

International Iberian Nanotechnology Lab…

24 PUBLICATIONS **248** CITATIONS

SEE PROFILE

Ulf Olsson

Lund University

269 PUBLICATIONS **7,005** CITATIONS

SEE PROFILE

Size, Shape, and Charge of Salt-Free Catanionic Microemulsion Droplets: A Small-Angle Neutron Scattering and Modeling Study

Bruno F. B. Silva,[†] Eduardo F. Marques,*,[†] Ulf Olsson,[‡] and Per Linse[‡]

Centro de Investigação em Química, Department of Chemistry, Faculty of Science, University of Porto, Rua do Campo Alegre n° 687, P 4169-007 Porto, Portugal, and Physical Chemistry, Center for Chemistry and Chemical Engineering, Lund University, P.O. Box 124, SE-221 00 Lund, Sweden

The formation and microstructure of a novel microemulsion based on a salt-free catanionic surfactant have been examined by considering the hexadecyltrimethylammonium octylsulfonate (TASo)−decane−D₂O system and using small-angle neutron scattering and self-diffusion NMR. With focus on the emulsification failure boundary, o/w discrete droplets have been observed and characterized for all of the studied microemulsion range. The evaluation of the experimental data was facilitated by using structure factors of a model system composed of charged particles interacting with a screened Coulomb potential. Furthermore, a more simplified model involving a charge regulation mechanism has been employed. Both approaches support the view that the droplets are mainly spherical, fairly monodisperse, and charged. The net charge of the surfactant film is a consequence of the partial dissociation of the short-chain counterpart, owing to its higher solubility. We have further quantified how the droplet charge varies with volume fraction and, from that dependence, explained the unusual phase behavior of the TASo−water system, a seldom found coexistence of two lamellar liquid−crystalline phases in a binary system. This coexistence is quantitatively modeled in terms of a fine balance between the attractive and repulsive colloidal forces acting within the system.

1. Introduction

Microemulsions, consisting of thermodynamicaly stable isotropic mixtures of oil and water stabilized by a surfactant,[1] find a broad range of technical applications, from detergency and petrochemical feedstocks[2] to food engineering,[3] drug delivery,[4] nanotemplate chemistry,[5] and inkjet technology.[6] The phase behavior of a microemulsion can be rationalized by the relative amounts of its three components and by the mechanical properties of the amphiphilic film, described within a flexible surface model. Here, the behavior is assumed to be governed by the curvature elasticity of the film and spontaneous curvature.[7−16] The Gibbs curvature energy can be written as[17]

$$G_c = \int \{2\kappa(H - H_o)^2 + \bar{\kappa}K\}dA \qquad (1)$$

where $H = (c_1 + c_2)/2$ and $K = c_1c_2$ are the mean and Gaussian curvatures, respectively, $c_1 = 1/R_1$ and $c_2 = 1/R_2$ are the two local principal curvatures, κ and $\bar{\kappa}$ are the bending and saddle-splay modulus, respectively, and H_o is the spontaneous curvature. If H_o is positive, the surfactant film curves toward oil (positive curvature) and forms o/w (oil-in-water) droplets, whereas if H_o is negative, the film curves toward water (negative curvature), and water-in-oil droplets are favored. If H_o is zero, a bicontinuous structure is formed.

Since all of the surfactants are preferentially located at the oil−water interface, the optimal radius for a spherical droplet, R_c, is dictated by the composition through[18]

$$R_c = 3(\Phi_o/\Phi_s + \alpha)(v_s/a_o) \qquad (2)$$

where Φ_o and Φ_s are the volume fractions of oil and surfactant, respectively, v_s is the molecular volume of the surfactant, a_o is its interfacial area in the film, and α accounts for the fact that the droplet volume has also a contribution from the thickness of the surfactant film.

There is a saturation limit where the droplets solubilize the maximum amount of oil. Further oil added will phase-separate, and the composition line where this occurs is known as the emulsification failure (EF) boundary. Here, the flexible surface model, neglecting the entropy of mixing, predicts that the micelles are spherical, with a radius R given by[19]

$$\frac{R}{R_0} = 1 - \frac{\bar{\kappa}}{2\kappa} \qquad (3)$$

which is practically equal to R_c. Here $R_0 = 1/H_0$. On the other hand, reducing the amount of oil reduces R_c. Because this value is now different from $1/H_0$, leading to an unfavorable film energy, the droplets will deform to prolates or elongated micelles in order to approximate H to H_0 and hence reduce the Gibbs curvature energy G_c.

For single-chained ionic surfactants, the film curvature is usually very high for oil to be incorporated, and generally, one has to decrease the spontaneous curvature to form microemulsions. This can be achieved by adding salt, a cosurfactant, or an oppositely charged surfactant to the system. In the latter case, some of the surfactant charge is neutralized, the hydrophobic portion increased, and thus H_o decreased. For catanionic mixtures[20−22] with excess ionic surfactant, o/w microemulsion droplets have been observed, as expected.[23−26] H_o continually

* To whom correspondence should be addressed. E-mail: efmarque@fc.up.pt.
    [†] University of Porto.
    [‡] Lund University.

Size, Shape, and Charge of Microemulsion Droplets

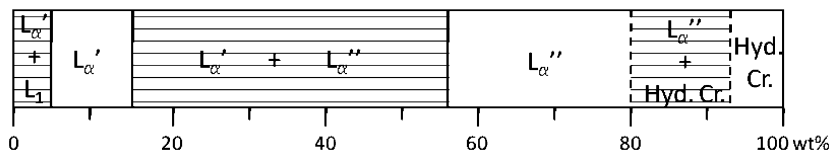*J. Phys. Chem. B, Vol. 113, No. 30, 2009* **10231**

Figure 1. Phase diagram of the binary TASo−water system at 25 °C containing isotropic solution (L_1), swollen lamellar phase (L_α'), collapsed lamellar phase (L_α''), and hydrated crystals (Hyd. Cr.) (adapted from ref 36).

decreases as the molar ratio between both individual surfactants approaches 1 (charge matching).

Microemulsions can also be prepared with neutral catanionic surfactants (with no salt present), such as those originally reported by Jokela, Khan, and Jönsson.[20−22] For bulky head groups (e.g., dodecyltrimethylammonium dodecylsulfate), o/w droplets form in the presence of charge, but no reverse phases are created due to the high stability of the neutral catanionic precipitate. In this case, reverse or bicontinuous can form by addition of a fourth component such as hexanol.[23,25] For small head groups (e.g., octylammonium octanoate), in turn, w/o reverse droplets readily assemble and grow upon addition of charge. Small-angle neutron scattering (SANS) and conducto-metric[27,28] studies have recently shown that for neutral catanionic surfactants, reverse spheres can form, growing initially to short cylinders and then to long semiflexible (or worm-like) reverse micelles as water is gradually added up to the EF boundary.

Most neutral catanionic compounds are insoluble in water at or near room temperature. Important exceptions include catan-ionics for which the anionic part is a carboxylate[29−32] or when at least one of the ionic counterparts is comparatively short-chained.[33,34] In particular, it has been recently observed that hexadecyltrimethylammonium octylsulfonate (TASo) is soluble at room temperature, yielding elongated micelles, vesicles,[35] and two coexisting lamellar phases in water at higher concentrations[36] (Figure 1). Since the two ionic parts of the compound have different solubilities, the most soluble one partially escapes to the bulk, leaving the catanionic surface with a net charge, according to the chemical equilibrium

$$TA_nSo_n(agg) \rightleftarrows (TA_nSo_{n-m})^{m+}(agg) + mSo^-(aq) \tag{4}$$
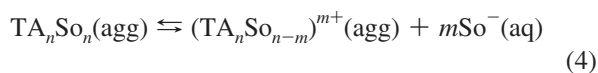
If the solubility of the short-chained surfactant is assumed to be independent of the surfactant concentration, the surface charge density increases by adding water to the system. This gives rise to a balance of forces that ultimately is responsible for both the lamellar−lamellar phase coexistence and the observed temperature-dependent micelle−vesicle transition. Even though this simple model has proven to be successful in predicting the global phase behavior, the excess solubility of octylsulfonate (So⁻) is still experimentally uncertain. It has previously been estimated to ∼20 mM from a fit of the miscibility gap using an equation of state.[36]

Because TASo aggregates are thought to be charged and the head groups are fairly bulky, formation of reverse w/o micro-emulsions can be excluded a priori. On the other hand, we recall that the neutral dodecytrimethylammonium dodecylsulphate (somewhat similar to TASo but with symmetric chain lengths) does not form any microemulsions. Thus, one of the motivations for this work is to examine the formation of o/w microemulsion droplets by TASo, an observation that by itself should further support the presence of charged aggregates. Furthermore, near the EF boundary, the presumptive o/w droplets should be spherical. This would allow one to model them as macroions

and quantify the charge (and hence, the excess solubility of So⁻) by comparison of model calculations with scattering data.

For this purpose, the phase behavior of the ternary TASo−decane−D₂O system has been investigated to search for the microemulsion region and the EF boundary. The micro-structure (shape and size) of the aggregates has been character-ized by SANS and complemented with self-diffusion NMR. Because it is often difficult to distinguish between polydisperse spheres and prolates along the EF boundary with SANS,[37,38] two different contrasts have been used to more firmly establish the droplet shape. Finally, since small-angle scattering data contains information on interparticle interactions,[39] a model has been developed to extract the droplet charge and the excess So⁻ solubility.

2. Experimental Section

2.1. Materials and Sample Preparation. Hexadecyltri-methylammonium bromide (CTAB), sodium octylsulfonate (SOSo), and decane were purchased from Sigma. Deuterated water and deuterated decane were purchased from Armar Chemicals. All of the chemicals were used as received. The catanionic TASo surfactant was obtained by mixing micellar solutions of CTAB and SOSo in equimolar proportions accord-ing to a procedure previously described.[40] The catanionic surfactant was obtained in excellent purity (elemental analysis) with only a vestigial trace of salt (sodium bromide).

For the phase diagram studies, samples were prepared by weighing appropriate amounts of TASo, decane, and D₂O, carefully mixing, and waiting for equilibrium to be attained (at least one week). The phase boundaries were determined by ocular inspection and, when necessary, with the help of cross polarizers. For the SANS measurements, the EF boundary samples were prepared by a dilution series of the most concentrated sample. To monitor the formation of the droplets at a fixed surfactant-to-water ratio but different o/s, two samples of 5 and 10 wt % TASo in water were prepared. Decane was added to the lamellar phase until the EF boundary was reached. The samples for NMR and density determination were aliquots of the same samples as those used for the SANS measurements. In order to match the contrast of D₂O and deuterated decane $C_{10}D_{22}$, a small amount (2.6%) of protonated decane $C_{10}H_{22}$ was added to $C_{10}D_{22}$. Surfactant density measurements were per-formed on an Anton Paar DMA 5000 densitimeter, yielding for TASo a specific mass of 0.977 kg dm⁻³.

2.2. Small-Angle Neutron Scattering Experimental De-tails. SANS measurements were performed in the SANS1 instrument[41] at the SINQ lab at the Paul Scherrer Institute (PSI), Switzerland. A range of scattering vectors q from 0.04 to 4.1 nm⁻¹ was covered by a combination of three sample-to-detector distances SDD (set1, SDD = 1.6 m; set2, SDD = 6 m; set3, SDD = 18 m) and one wavelength ($\lambda = 0.6$ nm). The wavelength resolution $\Delta\lambda/\lambda$ was 10% (fwhm). A detector with 128 × 128 pixels and a pixel size of 0.75 cm was used. The samples were kept in 1 or 2 mm quartz cells (Hellma). The two-dimensional isotropic scattering spectra was corrected for detector efficiency by dividing the scattering spectra from the

samples by the incoherent scattering spectra of pure water and, subsequently, was radially averaged and converted to absolute scale (BerSANS software[42]). The background scattering was then subtracted by subtracting the constant value of the incoherent scattering measured at high q values.

2.2.1. Data Evaluation Procedure. Small-angle neutron scattering is an optimal tool to determine size, shape, and charge of microemulsion droplets. The form factor $P(q)$ contains information on the particle size and shape, whereas the structure factor $S(q)$ contains information on the particle–particle interactions. $S(q)$ is highly dependent on polydispersity; thus, instead of using the simple monodisperse approximation, one has to calculate the total scattering intensity $I(q)$ according to

$$I(q) = \sum_{i=1}^{m} \sum_{j=1}^{m} \sqrt{n_i n_j} F_i(q) F_j(q) S_{ij}(q) \qquad (5)$$

where n_i is the number density of particles of type i, $F_i(q)$ is the form amplitude of a particle of type i, $S_{ij}(q)$ is the partial structure factor of the pair ij, and m is the number of particle types.

The form amplitude $F(q,R_1,R_2)$ of a spherical core–shell particle with an inner radius R_1 and an outer one R_2 is given by

$$F(q, R_1, R_2) = V_2 \Delta\rho_2 \left(\frac{3[\sin(qR_2) - qR_2 \cos(qR_2)]}{qR_2^3} \right) - V_1 \Delta\rho_1 \left(\frac{3[\sin(qR_1) - qR_1 \cos(qR_1)]}{qR_1^3} \right) \qquad (6)$$

where $\Delta\rho_1$ and $\Delta\rho_2$ are the scattering length density difference between the shell and core and the shell and the medium, respectively, and $V_k = (4\pi/3)R_k^3$, $k = 1$ and 2. The form factor $P(q)$ is simply the square of the form amplitude $F(q)$.

The structure factor $S(q)$ has information on the correlations between the particles and hence indirectly on the interparticle interactions and on the particle charge. However, there are only a few theories with simple particle potentials where an analytical solution exists for $S(q)$. Our data analysis strategy involved first a determination of the particle shape, size, and polydispersity through the fitting of $P(q)$, followed by subsequent calculations of $S(q)$ using the particle properties.

2.2.2. Form Factor Fit. The form factor $P(q)$ was fitted by using the SASfit software package.[43] For the fitting of spherical droplets, a model of spherical shells[44] has been used ("spherical shell iii" in SASfit), with a Gaussian size distribution. For fitting of prolates, the model "Ellipsoidal core shell structure" also present in SASfit was used. At this stage, the structure factor was ignored ($S(q) = 1$).

2.2.3. Structure Factor Fit. We recall that the droplet charge in the system is intrinsically related with the excess solubility of So^- relative to hexadecyltrimethylammonium (TA^+). For reasons that will be clear further, this excess solubility will be referred to as effective solubility, $[So^-]_{eff}$. The relation between the droplet charge Z and $[So^-]_{eff}$ is given by

$$Z = \Phi_w [So^-]_{eff} N_A / N_d \qquad (7)$$

where Φ_w is the water volume fraction, N_A is the Avogadro number, and $N_d = \Phi_d/V_d$ is the droplet number density with V_d being the droplet volume.

The structure factor $S(q)$ was obtained by solving the Ornstein–Zernike (OZ) equation using two different closures. A closure implies certain approximations in the determination of the solution structure. For instance, the hypernetted chain (HNC) closure is more accurate for long-range potentials, whereas the Percus–Yevick (PY) closure works better for short-range potentials. Considering the broad variation of droplet charge and volume fraction, we have employed both the HNC and PY closures. The Rogers–Young (RY) closure, continuously interpolating between the HNC and PY closures, was discarded since the empirical mixing parameter used to adjust the osmotic compressibility becomes a function of concentration, preventing the decoupling of that parameter and the droplet charge Z in the fittings.

From the form factor analysis with a Gaussian size polydispersity distribution, we obtained a size polydispersity, σ/R_d (where σ stands for standard deviation), of 0.13 and 0.10 for the bulk and the shell contrast, respectively. To account for this size polydispersity, the system was modeled as being composed of $m = 5$ types of droplets. The size distribution of the m droplet types was chosen in such a way that the first $2m - 1$ moments were the same as those for the continuous size distribution determined from the form factor.[39,45] The charges of the droplets were obtained from $[So^-]_{eff}$ through eq 7 and the assumption that the m types of droplets had the same surface charge density. The droplets were assumed to interact through a screened Coulomb potential,[46] with the screening length κ^{-1} determined from $[So^-]_{eff}$ and with sodium bromide present as a residual contamination (0.6% of the surfactant concentration).

By choosing a value of the fitting parameter $[So^-]_{eff}$, all other parameters characterizing the system can be derived, and the OZ equation with the appropriate closure was solved.[47] Finally, from the calculated partial structure factors S_{ij}, the total scattering intensity $I(q)$ was determined using eq 5, extended with a procedure taking into account experimental resolution effects.[48] We emphasize that data are fitted on an absolute intensity and that the effective solubility $[So^-]_{eff}$ was the only fitting parameter. The value of $[So^-]_{eff}$ that yielded the best fit was taken as the effective solubility for that given concentration.

2.3. Pulsed Field Gradient Self-Diffusion NMR. Self-diffusion of alkyl protons on TASo and decane was measured at 25.0 °C using a 200 MHz Bruker DMX200, equipped with a diffusion probe with a maximum field gradient of 9 T m^{-1}. The typical pulsed field gradient NMR sequence was based on a stimulated echo sequence and is described in detail elsewhere.[49,50] If we have closed droplets, the diffusion coefficient D of TASo and decane can be taken as the diffusion coefficient D of the droplets. If droplet–droplet interaction can be neglected, the hydrodynamic radius R_H of the droplets is given through the Stokes–Einstein equation[51,52]

$$R_H = \frac{kT}{6\pi\eta D} \qquad (8)$$

where k is the Boltzmann constant, T is the absolute temperature, and η is the viscosity of the medium.

3. Results and Discussion

3.1. Phase Behavior and Microstructure in the TASo–Water–Decane System. After mixing a 5.0 wt % sample of TASo with a 1:1 mixture of heavy water and decane, a milky emulsion forms, developing after some days into a two-phase region of a clear isotropic microemulsion phase on the bottom and excess decane on the top. This simple observation indicates
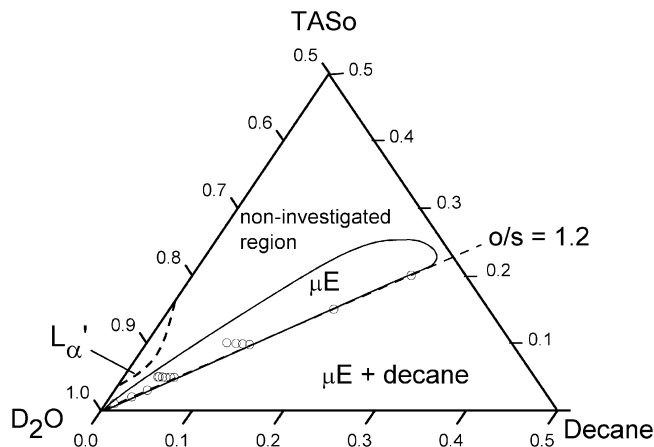
Size, Shape, and Charge of Microemulsion Droplets

J. Phys. Chem. B, Vol. 113, No. 30, 2009 **10233**

Figure 2. Phase diagram of the ternary TASo−water−decane system in the water-rich corner displaying the extension of a microemulsion phase (μE), the approximate extension of a swollen lamellar phase (L_α'), and microemulsion samples studied by SANS (open circles). The EF boundary occurring at o/s = 1.2 for high Φ_d is given (dashed line).

that TASo forms normal o/w microemulsions and has a spontaneous curvature that is positive toward oil (our convention). This behavior is in contrast with that of catanionic surfactants with smaller head groups, where reverse microemulsion droplets were observed.[27,28,53] It is also different from that of neutral catanionic surfactants of very similar head groups but with chains of equal length, such as dodecyltrimethylammonium dodecylsulfate (TAS), where a normal o/w microemulsion is found when charge is added.[24] Thus, the reason why TASo is soluble in water and forms o/w microemulsions stems indeed from an excess charge, originating from the large differences in the solubility of both ionic parts.

The phase diagram of the TASo−water−decane ternary system given in Figure 2 gives more detailed information on the phase behavior and on the microemulsion formation. The sample composition is henceforth expressed by the oil-to-surfactant ratio (o/s) and droplet volume fraction Φ_d (the sum of TASo and decane volume fractions, $\Phi_s + \Phi_o$). The microemulsion lobe is present in the water-rich corner of the phase diagram, extending from an o/s ratio of ∼0.7−1.2, the latter ratio being the EF boundary. The o/s ratio is almost constant over the whole EF boundary, except at small Φ_d, where it moves to a smaller o/s ratio. At o/s values above the EF boundary, excess oil and normal microemulsion droplets coexist; reverse droplets are not observed. At o/s ratios below 0.7 and at low Φ_d, the microemulsion coexists with the swollen lamellar phase L_α' that incorporates some oil. At higher Φ_d, the microemulsion coexists with the two lamellar phases. Here, the phase behavior is complex and has not been investigated in detail.

The shape and size of droplets formed were determined by using two contrasts. The use of several contrasts is a technique suitable to distinguish between shape and size polydispersity.[37,38] Figure 3 shows the two contrasts used. In the bulk contrast, the oily core and surfactant film have almost identical scattering lengths, and thus, the neutrons experience this droplet roughly as a solid sphere. In the shell contrast, the deuterated decane has a scattering length very similar to that of the solvent, and thus, the neutrons experience the droplet as a hollow shell. The scattering length densities of 6.37×10^{-4} nm^{-2} for D$_2$O, -1.45×10^{-5} nm^{-2} for TASo, -4.88×10^{-5} nm^{-2} for decane, and 6.58×10^{-4} nm^{-2} for deuterated decane were obtained from NIST.[54] The scattering length density of deuterated decane was adjusted to 6.47×10^{-4} nm^{-2} by addition of 1.6% of protonated
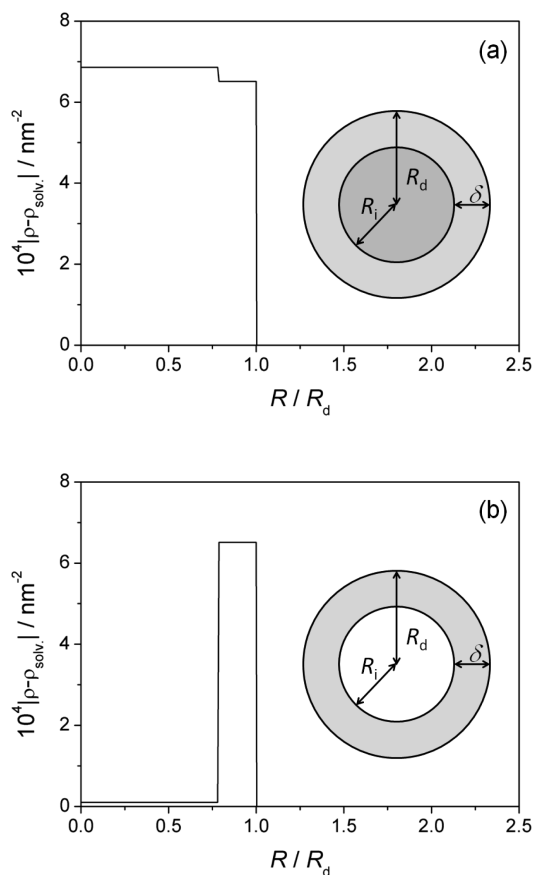

Figure 3. Scattering length density radial profile for (a) bulk and (b) shell contrasts. The insets are schematic representations of the droplet contrasts, where R_i is the radius of the oil core, R_d is the radius of the droplet, and δ is the thickness of the surfactant film.

decane. In the region along the EF boundary, both bulk and shell contrasts were applied, whereas away from the EF boundary, only bulk contrast was used.

3.1.1. EF Boundary. The obtained scattering data of the samples along the EF boundary are displayed in Figure 4. Noticeable is the large influence of the structure factor on the total scattering at low q, even at volume fractions as low as 4.4%. This is a direct consequence of the charge of the droplets. To obtain the droplet size and shape, this low-q part (typically $q < 0.4$ nm^{-1}) has to be excluded in the fitting of the form factor. Furthermore, the bulk contrast is fairly insensitive to the shell thickness δ due to the very small scattering length differences between the protonated oil and surfactant. Thus, δ was first obtained in the shell contrast and then used as a fixed parameter when fitting the bulk contrast data.

The best fits of the form factor using the spherical core−shell are also displayed in Figure 4 (solid curves). Neglecting the low-q part, the fits are extremely good, confirming that the droplets indeed are spherical. The fitted droplet parameters are displayed in Table 1. Along the EF boundary at the droplet volume fraction range of $0.044 < \Phi_d < 0.44$ and in both contrasts, we find that the droplet size is essentially constant. The obtained shell thickness of 1.7 nm is slightly larger than half of the bilayer thickness observed for lamellae in the binary system.[36] The increased thickness is attributed to penetration of oil in the surfactant layer. The average radius is 7.5 nm for bulk contrast and 7.6 nm for shell contrast, whereas the size polydispersity is 0.13 for bulk contrast and 0.10 for shell contrast. At the smallest droplet concentration, $\Phi_d = 0.019$ (o/s = 0.9), the obtained radius is smaller, namely, 6.4 nm.
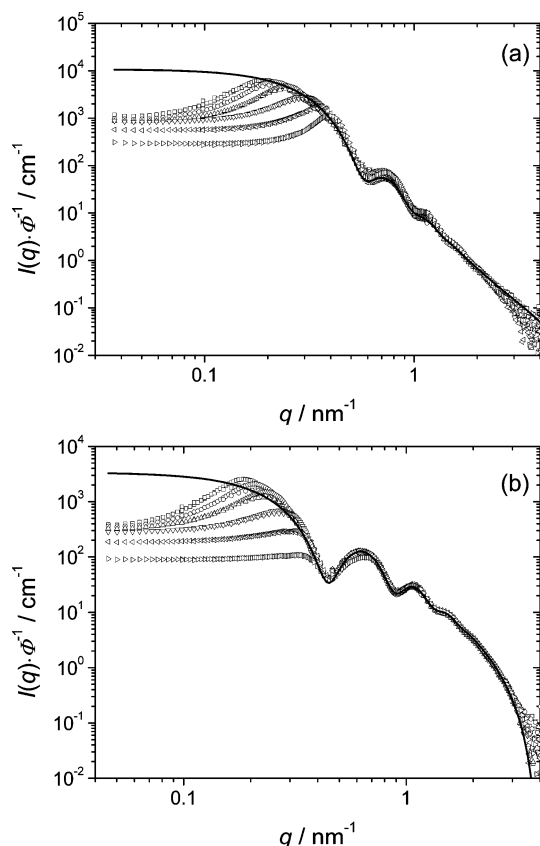
10234 *J. Phys. Chem. B, Vol. 113, No. 30, 2009*

Silva et al.

Figure 4. Droplet SANS data along the EF boundary for (a) bulk and (b) shell contrasts at Φ_d = 0.044, 0.066, 0.11, 0.22, 0.33, and 0.44 (symbols, top to bottom) and calculated unscaled form factors predicted from a spherical shell with thickness δ = 1.7 nm and outer radii R_d = 7.5 (bulk contrast) and 7.6 nm (shell contrast).

TABLE 1: Droplet Structural Parameters at the EF Boundary[a] Obtained from SANS Data Fitting

	bulk		shell		
Φ_d	R_d/nm	σ/R_d	R_d/nm	σ/R_d	δ/nm
0.019	6.4	0.13			
0.044	7.5	0.13	7.6	0.10	1.7
0.066	7.5	0.13	7.6	0.10	1.6
0.11	7.5	0.14	7.6	0.11	1.7
0.22	7.5	0.16	7.6	0.10	1.7
0.33	7.5	0.13	7.6	0.10	1.7
0.44	7.5	0.11	7.5	0.10	1.6
average	7.5	0.13	7.6	0.10	1.7

[a] The o/s = 1.2, except for Φ_d = 0.019 where o/s = 0.9.

The NMR diffusion coefficients for TASo and decane are identical, further confirming the discrete-type structure, where the two components diffuse together. Figure 5 shows a linear dependence of D on Φ_d, with the best fit (solid line) to $D/D_0 = 1.0 - \alpha\Phi_d$, yielding $D_0 = 2.2 \times 10^{-11}$ m²s⁻¹ and α = 2.0. From the diffusion coefficient at infinite dilution (D_0) and eq 8, a hydrodynamic radius of R_H = 8.6 nm is obtained. This value is 15% higher than R_d from SANS, which can be explained by the fact that R_H also contains contributions from dragged solvent molecules. Thus, the self-diffusion data agree extremely well with SANS with respect to the presence of discrete droplets and their size. The fit is very close to that expected for hard spheres, $D/D_0 = 1.0 - \alpha_S\Phi_d$, where α_S = 2.1 if hydrodynamic interactions are included and α_S = 2.0 if they are excluded.[55] This observation is consistent with the low charge of the
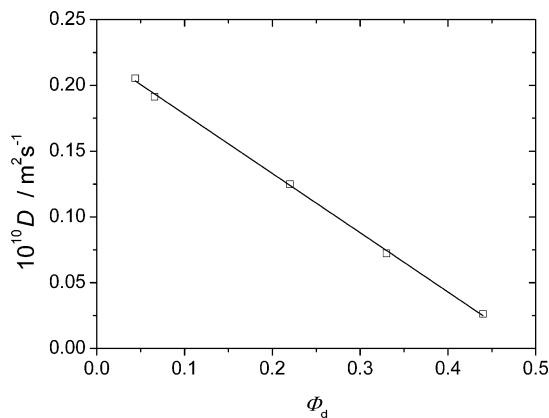

Figure 5. Droplet self-diffusion coefficient (as inferred from TASo and decane self-diffusion) as a function of droplet volume fraction, Φ_d. The solid line is a linear fit to the equation $D/D_0 = 1.0 - \alpha\Phi_d$, with $D_0 = 2.2 \times 10^{-11}$ m² s⁻¹ and α = 2.0.
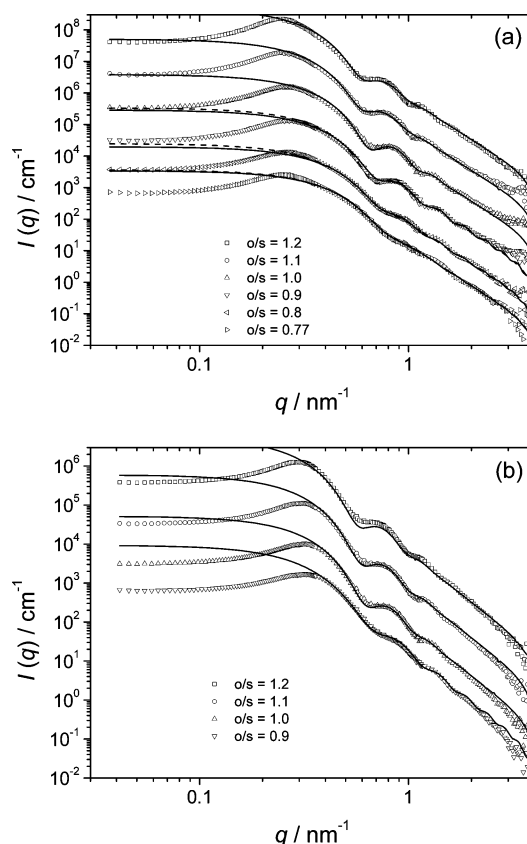

Figure 6. Droplet SANS data with bulk contrast for X_s = (a) 0.05 and (b) 0.10 at indicated values of o/s (symbols) and best fitted form factors using spherical (solid curves) and prolate (dashed curves) droplets. For clarity, the scattering curves are displaced vertically by factors of 5×10^x, with x = 0, 1, 2, 3, 4, and 5 from bottom to top.

droplets, and it has been also previously found for nonionic microemulsions doped with small surface charges.[46]

3.1.2. Away from the EF Boundary. Compositions away from the EF boundary were achieved by fixing the TASo concentration in water ($X_s = \Phi_s/(\Phi_s + \Phi_w)$) and gradually decreasing the oil-to-surfactant ratio (see Figure 2). Scattering data at X_s = 0.05 and 0.10 for various oil-to-surfactant ratios are displayed in Figure 6, and results of the best fits are given in Table 2.

In general, at decreasing o/s ratio, the droplets shrink but maintain their spherical shape until o/s = 0.9 at X_s = 0.05 and o/s = 1.0 at X_s = 0.1. Below these o/s values, best fits are

Size, Shape, and Charge of Microemulsion Droplets

J. Phys. Chem. B, Vol. 113, No. 30, 2009 **10235**

TABLE 2: Droplet Structural Parameters Away from the EF Boundary Obtained from SANS Data Fitting[a] and the Apparent Hydrodynamic Radius $R_{H,ap}$ Obtained from Self-Diffusion NMR[b]

| | sphere | | | NMR | prolate | | | |
| | SANS | | | | SANS | | | |
X_s	o/s	R_d/nm	σ/R_d	$R_{H,ap}$	R_{dM}/nm	R_{dm}/nm	$\sigma_{R_{dm}}/R_{dm}$	R_{dM}/R_{dm}
0.05	1.1	7.1	0.15	8.4				
	1.0	6.7	0.12	7.7				
	0.90	6.4	0.12	7.2				
	0.80	*5.2*	0.25	12	7.0	4.7	0.29	1.5
	0.77	*4.8*	0.26	19	7.8	4.6	0.20	1.7
0.10	1.1	7.2	0.14	6.7				
	1.0	6.9	0.14	7.6				
	0.90	*6.3*	0.20	11	6.4	5.0	0.41	1.1

[a] The shell thickness was fixed to $\delta = 1.7$ nm for both spherical and prolate shapes. The values in italic are fits where an enhanced polydispersity was obtained (see text). [b] The diffusion coefficients from which $R_{H,ap}$ was obtained (Figure 7) were corrected to infinite dilution (D_0) by use of the equation $D/D_0 = 1 - 2.0\Phi_d$.
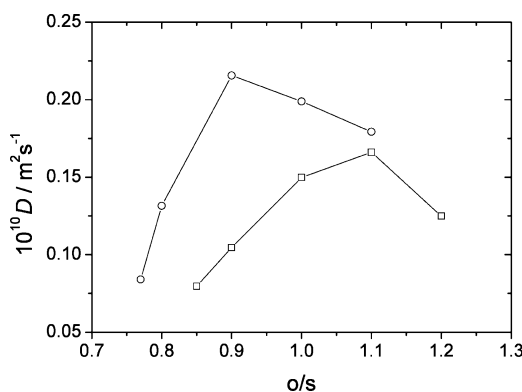

Figure 7. Droplet self-diffusion coefficient (as inferred from decane and TASo self-diffusion) versus the oil-to-surfactant ratio at $X_s = 0.05$ (circles) and 0.10 (squares).

obtained with a prolate shape with a polydispersity in the minor radius ($\sigma_{R_{dm}}$). If insisting upon a spherical shape, the fittings were still good but resulted in an increased size polydispersity. Hence, care must be taken. It is well-known that the same form factor can be obtained for polydisperse spheres and prolates,[56] and the clear distinction between both shapes is possible with a contrast variation technique.[37,38]

The separation of the shape and polysperdity interdependence can be addressed with the self-diffusion NMR technique.[57] Figure 7 shows the self-diffusion coefficients D obtained at $X_s = 0.05$ and 0.10 as a function of the o/s ratio. A decrease in the o/s ratio leads first to an increase in D, while after o/s = 0.9 at $X_s = 0.05$ and after o/s = 1.1 at $X_s = 0.10$, D decreases again. We interpret this effect in the following way: initially, there's a decrease in R_H while the spherical shape is kept, and afterward, a unidimensional growth occurs, probably to a prolate shape, resulting in an increased R_H and a concomitant reduced D. We recall that R_H is larger for a prolate than for a sphere of the same volume.[58] An apparent hydrodynamic radius, $R_{H,ap}$, can be estimated by the use of both the expression obtained for the EF boundary, $D/D_0 = 1.0 - 2.0\Phi_d$, implying the assumption of a hard-sphere-type behavior here as well, and eq 8. As can be seen in Table 2, when D increases (Figure 7), $R_{H,ap}$ decreases, and the values are in good agreement with SANS (slightly larger due to the solvent effects). When D starts to decrease at the inflection point, $R_{H,ap}$ increases abruptly, in sheer contrast with the SANS data. This discrepancy indicates that the spherical model is no longer valid and is thus a qualitative and consistent indication of a shape change, being also supported by similar observations in nonionic microemulsion systems.[57]

In summary, even though SANS data, per se, are not enough to distinguish between prolates and spheres, they give indication of structural changes below a certain o/s ratio, and self-diffusion NMR confirms this picture. It should be kept in mind that in the framework of curvature energy (eq 1), this is the expected behavior when moving away from the EF boundary to smaller o/s ratios. A smaller amount of oil implies a decrease in droplet volume. Thus, the curvature starts to decrease and move away from its optimal value H_0. A way of minimizing this energetic penalty is to deform the droplets from spheres to prolates since the average curvature becomes smaller. This effect should be stronger for the higher volume fractions ($X_s = 0.10$) since at higher concentrations, the curvature energy is more dominant over entropy, which favors the maximum number of droplets, and consequently, spherical droplets.

3.2. Droplet Charge at the EF Boundary. Through the structure factor $S(q)$, the scattering at low q provides information on the spatial correlations between the droplets and, thus, on their charge. As mentioned above, the droplet charge Z is suggested to arise from the different solubilities of the ionic constituents of TASo.

We have been able to fit the scattering intensity $I(q)$ in the full q range by using partial structure factors obtained from the HNC and PY equations and thereby estimate the excess effective solubility $[So^-]_{eff}$ and consequently obtain the droplet charge Z through eq 7. Results of the best fits for some representative measurements are shown in Figure 8, and the overall fitting results are listed in Table 3.

Figure 8 shows that the fitted scattering curves describe the experimental data well, considering a single fitting parameter and that the data are fitted on an absolute scale. The quality of the fit is good for the bulk contrast, but some deviations can be seen for the shell contrast at lower q. This discrepancy is probably due to polydispersity effects that are not fully taken into account in the present simple model. In Figure 8c, the fitted first minimum of the form factor is overestimated. This is due to the fact that for this concentration, the measured polydispersity is slightly higher than the average (Table 1), while charge determination was performed by fixing this parameter to its average value ($\sigma/R_d = 0.13$ for bulk and $\sigma/R_d = 0.10$ for shell contrast).

The HNC and PY equations are able to fit the data equally well. However, different optimal values of $[So^-]_{eff}$ and Z are obtained; see Table 3. The HNC equation always gives larger $[So^-]_{eff}$ and Z than the PY equation. Since the HNC equation is more reliable for long-range potentials and the PY equation for short-range potentials, we consider the HNC equation more
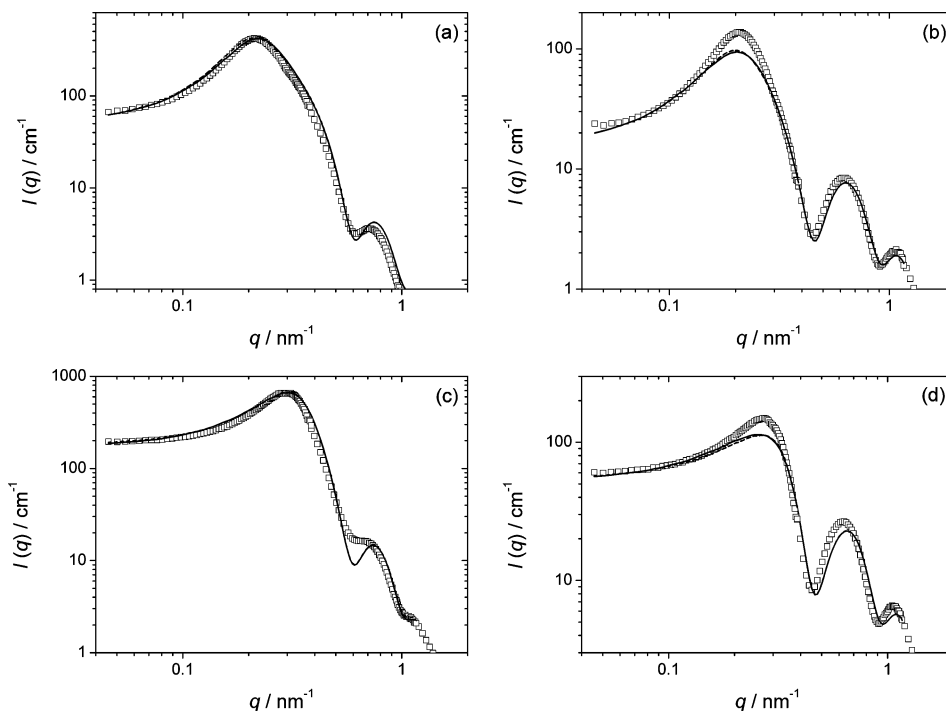
Figure 8. Scattering intensity at (a) $\Phi_d = 0.066$ and bulk contrast; (b) $\Phi_d = 0.066$ and shell contrast; (c) $\Phi_d = 0.22$ and bulk contrast; and (d) $\Phi_d = 0.22$ and shell contrast. Symbols are experimental points, and curves are best fits by using the HNC (solid curves) and PY (dashed curves) equations (in most cases, the solid and dashed curves are not distinguishable). Fitted $[So^-]_{eff}$ are given in Table 3.

TABLE 3: Predicted Effective Solubility $[So^-]_{eff}$ and Corresponding Droplet Charge Z Obtained from Fits to Total Scattering Intensity Using the HNC and PY Equations and the Charge Regulation (CR) Model (eqs 9a and 10) for Intrinsic Solubilities $[So^-]_0$ of 3.0 (bulk contrast) and 2.5 mM (shell contrast)

| | $[So^-]_{eff}$/mM | | | | | | Z | | | | | |
| | bulk | | | shell | | | bulk | | | shell | | |
Φ_d	HNC	PY	CR	HNC	PY	CR	HNC	PY	CR	HNC	PY	CR
0.019	0.55	0.42	1.0				31	23	35			
0.044	1.2	0.82	1.4	1.0	0.75	1.3	28	19	34	24	18	30
0.066	1.8	1.2	1.8	1.4	1.1	1.6	28	18	27	22	16	24
0.11	2.9	2.0	2.2	2.1	1.6	1.9	26	17	19	18	14	17
0.22	4.5	2.9	2.7	3.7	2.5	2.3	17	11	10	14	9.6	8.7
0.33	8.0	3.7	2.8	5.5	2.2	2.4	18	8.2	6.3	12	4.9	5.3

appropriate at low surfactant concentration, where the droplet charge is large, and consequently, the PY approximation is better at high surfactant concentration, where the hard-sphere interaction dominates over the electrostatic interaction.

Table 3 and Figure 9 provide fitted $[So^-]_{eff}$, the corresponding droplet charge obtained by eq 7 is given in Table 3, and the corresponding average charge density is given in Figure 9. Despite the quantitative difference, Figure 9 shows that the HNC and PY approximations yielded the same qualitative picture: the effective solubility decreases and the droplet charge increases when the surfactant concentration decreases. The combination of the most reliable points (filled symbols) of both closures yielded a better agreement with further model calculations, as explained in the following section.

3.3. Charge Regulation Model. Figure 9 shows that $[So^-]_{eff}$ decreases with decreasing Φ_d. At first glance, one could expect the excess solubility to be constant irrespectively of Φ_d. However, when the system is diluted, the increased amount of water extracts more So^- from the droplets, and thus, the droplet charge is increased. This effect enhances the effective repulsion among the charges residing on the droplet surface, hence tending to counteract the increase in $[So^-]$. At dilution, even though the amount of So^- in the bulk increases, $[So^-]$ diminishes. In

this sense, one should refer to this concentration as an effective solubility, $[So^-]_{eff}$, to distinguish it from the intrinsic solubility, $[So^-]_0$, occurring in the absence of this electrostatic penalty. With this background, we will derive a relationship between $[So^-]_0$ and $[So^-]_{eff}$ based on a charge regulation (CR) mechanism.[18]

Let us consider an ensemble of oil droplets in a salt-free aqueous solution of equimolar amounts of TA^+ and So^- surfactants. All of the surfactants should reside in the oil−water interface, except a small amount of So^-, which is assumed to have a finite solubility in water. For simplicity, TA^+ is assumed to have zero solubility. Ideally, the solubility of So^- should be independent of the surfactant concentration and remain constant throughout the whole composition range. This would increase the droplet charge Z (according to eq 4) when the surfactant concentration is lowered (dashed line in Figure 9). However, for every So^- molecule that leaves the droplet surface, an ionic charge is created on the surface, hence giving rise to an electrostatic energy penalty. Thus, if one considers the chemical potentials of the three species

$$\mu_{TAS_o} = \mu^\circ_{TAS_o} + kT \ln X_{TASo} \qquad (9a)$$

Size, Shape, and Charge of Microemulsion Droplets

J. Phys. Chem. B, Vol. 113, No. 30, 2009 **10237**

$$\mu_{TA^+} = \mu_{TA^+}^\circ + kT \ln X_{TA^+} + ze\Phi_0 \qquad (9b)$$

$$\mu_{So^-} = \mu_{So^-}^\circ + kT \ln[So^-] \qquad (9c)$$

and an intrinsic equilibrium constant for the surfactant dissociation (without the electrostatic contribution), given by

$$-kT \ln K_s^\circ = \Delta G^\circ = \mu_{TA^+}^\circ + \mu_{So^-}^\circ - \mu_{TASo}^\circ \qquad (10)$$

by realizing that in equilibrium (eq 4), the chemical potentials are equal for the left- and right-hand sides

$$\mu_{TA^+} + \mu_{So^-} = \mu_{TASo} \qquad (11)$$

one comes to

$$K_s = \frac{X_{TA^+}[So^-]}{X_{TASo}} = K_s^\circ \exp\left(\frac{-ze\Phi_0}{kT}\right) \qquad (12)$$

which yields the real equilibrium constant K_s, different from the intrinsic equilibrium constant K_s°. From K_s, one can extract both the surface charge and bulk concentration of So^-, that is, $[So^-]_{eff}$. Here, μ_i is the chemical potential of species i, k is the Boltzmann constant, X_i is the molar fraction of component i, z is the ion valency, e is the charge of the electron, Φ_0 is the surface potential, and $[So^-]$ is the concentration of So^-.

In our case, since all of the surface charge comes directly from the excess solubility, X_{TA^+} and the droplet charge Z can easily be related to each other from simple geometrical arguments through

$$X_{TA^+} = ZA_s/A_d \qquad (13)$$

where A_s is the molecular surface area and A_d is the droplet surface area. Since for moderate values of the excess solubility X_{TA^+} is small, then $X_{TASo} \approx 1$, and eq 12 can be converted (also bearing in mind eq. 7) to the convenient form

$$[So^-]_{eff} = \sqrt{[So^-]_0^2 \exp\left(\frac{-ze\Phi_0}{kT}\right)} \qquad (14)$$

which gives the relation between $[So^-]_{eff}$ and $[So^-]_0$. The charge is simply the number of bulk So^- molecules divided by the number of droplets, as previously mentioned, through eq 7.

The effective solubility $[So^-]_{eff}$ can then be obtained iteratively by using eq 14 for a given value of the intrinsic solubility $[So^-]_0$, where the surface potential Φ_0 is obtained numerically by solving the PB equation,[59,60] until convergence in $[So^-]_{eff}$ and Φ_0 is obtained. The modeled intrinsic solubility that best fits the scattering data is 3.0 and 2.5 mM for bulk and shell contrast, respectively.

The predicted $[So^-]_{eff}$ values from the CR model obtained by eqs 14 and 7 are also displayed in Figure 9 (solid curves). The predicted $[So^-]_{eff}$ becomes equal to $[So^-]_0$ at high Φ_d but becomes smaller as Φ_d decreases, owing to the charge regulation mentioned above. Figure 9 shows that the surface charge density increases at decreasing Φ_d; however, the increase is smaller than that if $[So^-]_{eff}$ would remain constant (dashed curves).

Thus, even with the CR mechanism, the droplet charge is increasing upon dilution, which should increase the spontaneous curvature H_0. This effect is negligible in most of the concentration ranges studied, but at very high dilutions, it starts to be significant. This is reflected by the constant droplet radius and EF boundary until $\Phi_d = 0.02$; below this value, the charge
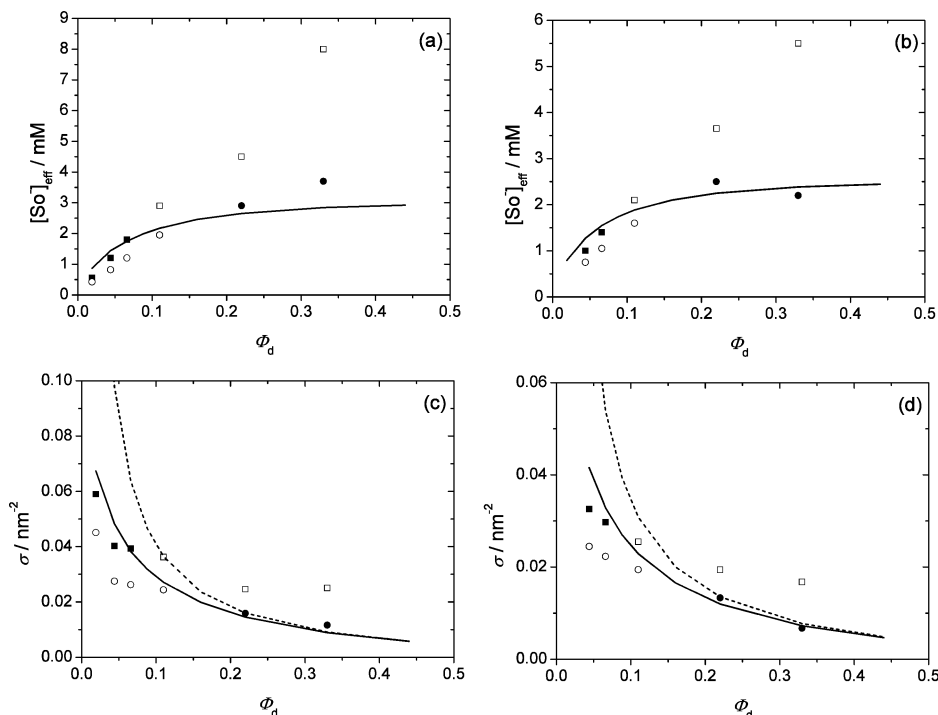

Figure 9. Predicted effective solubility $[So^-]_{eff}$ and corresponding charge density σ as a function of Φ_d from fits to scattering intensity using the HNC (squares) and PY (circles) equations; (a) $[So^-]_{eff}$ with bulk contrast, (b) $[So^-]_{eff}$ with shell contrast, (c) σ with bulk contrast, and (d) σ with shell contrast. Symbols are filled in the regime where the corresponding closure is better than the other one. Results from the charge regulation model with $[So^-]_0 = 3.0$ mM for bulk contrast and $[So^-]_0 = 2.5$ mM for shell contrast (solid curves) and results in the absence of a charge regulation mechanism (dashed curves) are also given.

growth starts to be effective in increasing H_0, and, therefore, at this point, the EF boundary shifts to lower o/s values (smaller droplets).

A comparison of (i) the fitted values of the charged particle model solved by using the HNC and PY equations and (ii) the values obtained from the CR model given in Figure 9 shows reasonable agreement. In particular, the predictions of the CR model (solid curves) are close to the solid points, considered to be the most reliable combination of the HNC and PY equations. It is worth mentioning here that there are approximations in each of the theories, making the overall result satisfactory.

In summary, the intrinsic solubility of the sulfonate part in TASo is ~3 mM, which is smaller than 20 mM previously proposed for the miscibility gap modeling of the binary TASo−water system.[36] In that study, the solubility was assumed to be constant through the whole composition region, that is, a charge regulation mechanism was not included. We are therefore now in a position to refine the equation of state of the binary TASo−water system.

3.4. Binary TASo−Water System: The Lamellar Miscibility Gap Revisited. It has been shown that the relation between charge density and excess solubility in the TASo−water system is given by[36]

$$\sigma = \frac{1}{2}[\text{So}^-]_{\text{aq}}\delta\left(\frac{1}{\Phi_s} - 1\right) \tag{15}$$

with the difference that now, $[\text{So}^-]_{\text{aq}}$, the concentration of octylsulfonate ions in the water layer is identified with $[\text{So}^-]_{\text{eff}}$ and obtained through eq 14. Here, δ is the bilayer thickness. Equation 14 is again iteratively solved with the charge density given by eq 15 and the surface potential Φ_0 calculated through the PB equation solution for two parallel charged plates.[61] Within this PB solution, the electrostatic contribution to the osmotic pressure Π_{el} is calculated by[18]

$$\Pi_{\text{el}} = \frac{2(kT)^2\varepsilon_r\varepsilon_0}{(ze)^2}\left(\frac{2s}{d - \delta}\right)^2 \tag{16}$$

where $d = \delta/\Phi_s$ is the lamellar repeat distance, ε_r is the relative dielectric constant of the medium, ε_0 is the vacuum permittivity, and s is given by the transcendental equation

$$s\tan(s) = -\frac{ze\sigma(d - \delta)}{4kT\varepsilon_r\varepsilon_0} \tag{17}$$

In the description of lamellar stacks in the full concentration range, the attractive van der Waals, Π_{vdW}, and short-range repulsion, Π_{SRR}, contributions should be also included, and these can be obtained through the derivatives of the equivalent potentials in ref 62 according to

$$\Pi_{\text{vdW}} = \frac{H}{12\pi}\left(\frac{4}{d^3} - \frac{2}{(d + \delta)^3} - \frac{2}{(d - \delta)^3}\right) \tag{18}$$

$$\Pi_{\text{SRR}} = a\exp(-(d - \delta)/\lambda) \tag{19}$$

where H is the Hamaker constant (here, fixed to 6×10^{-21} J, a reasonable value for lipid and surfactant bilayers); a is the force amplitude, generally between 10^6 and 10^8 N·m^{-2} (here, fixed
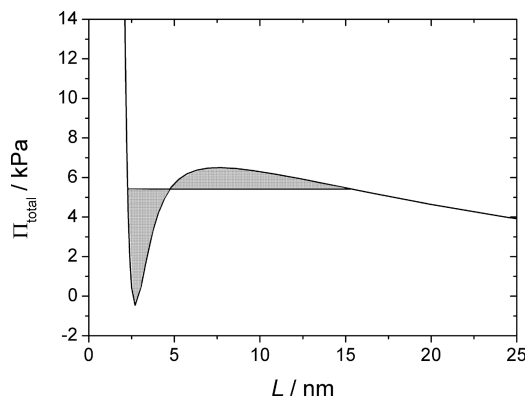

Figure 10. Total osmotic pressure versus interlamellar spacing for the binary TASo−water system using the charge regulation model for planar symmetry and an intrinsic solubility $[\text{So}^-]_{\text{eff}} = 3$ mM, $H = 6 \times 10^{-21}$ J, $A = 4 \times 10^7$ N·m^{-2}, and $\lambda = 0.3$ nm. The van der Waals loop implies a miscibility gap where two different lamellar phases with different spacings exist. The Maxwell construction (shaded areas) gives a miscibility gap in the interval of 15−54 wt % in surfactant.

at 4×10^7 N·m^{-2}); and λ is the decay length (here, 0.3 nm). As an additional simplification, the three contributions are considered to be additive

$$\Pi_{\text{total}} = \Pi_{\text{el}} + \Pi_{\text{vdW}} + \Pi_{\text{SRR}} \tag{20}$$

Calculating the total osmotic pressure Π_{total} with an intrinsic solubility of 3.0 mM (the obtained value in the previous section for bulk contrast) yields a Π_{total} versus interlamellar spacing $L = (d - \delta)$ curve with a van der Waals loop (Figure 10), implying a miscibility gap. A Maxwell construction allows the extraction of the limits for this gap, which become 54 and 15 wt % for the collapsed and swollen lamellar phases L_α'' and L_α' respectively, in outstanding agreement with boundaries of 54 and 15 wt % found for the experimental phase diagram (cf. Figure 1).

The deeper significance of these results is that both the binary TASo−water and ternary TASo−water−decane systems have their phase behavior explained within the framework of the same theory, based on the solubility mismatch and the charge regulation mechanism.

4. Conclusions

It has been shown that hexadecyltrimethylammonium octylsulfonate (TASo) forms an o/w microemulsion with decane and water. The microemulsion phase behavior has been mapped, and its EF boundary was localized at an oil-to-surfactant ratio of 1.2 for most of the phase diagram. At small droplet volume fractions, the EF boundary shifts to smaller o/s ratios as a result of the increasing droplet charge with dilution.

The microstructure of the droplets was determined by a combination of SANS and self-diffusion NMR. Along the EF boundary, the droplets are spherical, but away from it, prolate shapes are suggested to exist. The charge of the droplets has been determined through structure factor calculations and the intrinsic solubility of So$^-$ in water, accordingly set to be ~3 mM. This solubility (when compared with the much smaller TA$^+$ solubility) is responsible for TASo-rich phase behavior both in water and water + oil systems. The EF boundary (and its shift at smaller droplet volume fractions) is suggested to be also governed by this value.

Size, Shape, and Charge of Microemulsion Droplets

J. Phys. Chem. B, Vol. 113, No. 30, 2009 **10239**

The lamellar miscibility gap experimentally observed for the binary TASo−water system in a previous report has been recalculated using the new charge regulation model, and an excellent agreement was found, further supporting the physical picture behind the phase behavior in the ternary TASo−water−decane and in binary TASo−water systems.

References and Notes

(1) Danielsson, I.; Lindman, B. *Colloids Surf.* **1981**, *3*, 391.

(2) Verruto, V. J.; Kilpatrick, P. K. *Langmuir* **2008**, *24*, 12807.

(3) Flanagan, J.; Singh, H. *Crit. Rev. Food Sci. Nutr.* **2006**, *46*, 221.

(4) Heuschkel, S.; Goebel, A.; Neubert, R. H. H. *J. Pharm. Sci.* **2007**, *97*, 603.

(5) Hopwood, J. D.; Mann, S. *Chem. Mater.* **1997**, *9*, 1819.

(6) Magdassi, S.; Ben-Moshe, M.; Berenstein, L.; Zaban, A. *J. Imaging Sci. Technol.* **2003**, *47*, 357.

(7) Andelman, D.; Cates, M. E.; Roux, D.; Safran, S. A. *J. Chem. Phys.* **1987**, *87*, 7229.

(8) Leung, R.; Shah, D. O. *J. Colloid Interface Sci.* **1987**, *120*, 320.

(9) Lee, L. T.; Langevin, D.; Meunier, J.; Wong, K.; Cabane, B. *Prog. Colloid Polym. Sci.* **1990**, *81*, 209.

(10) Langevin, D. *Adv. Colloid Interface Sci.* **1991**, *34*, 583.

(11) Olsson, U.; Wennerström, H. *Adv. Colloid Interface Sci.* **1994**, *49*, 113.

(12) Strey, R. *Colloid Polym. Sci.* **1994**, *272*, 1005.

(13) Daicic, J.; Olsson, U.; Wennerström, H. *Langmuir* **1995**, *11*, 2451.

(14) Gradzielski, M.; Langevin, D.; Farago, B. *Prog. Colloid Polym. Sci.* **1996**, *100*, 162.

(15) Hellweg, T.; Langevin, D. *Phys. Rev. E* **1998**, *57*, 6825.

(16) Safran, S. A. *Adv. Phys.* **1999**, *48*, 395.

(17) Helfrich, W. *Naturforscher* **1973**, *28c*, 693.

(18) Evans, D. F.; Wennerström, H. *The Colloidal Domain: where physics, chemistry, biology and technology meet*, 2nd ed.; John Wiley & Sons, Inc: New York, 1999.

(19) Safran, S. A. *Phys. Rev. A* **1991**, *43*, 2903.

(20) Jokela, P.; Jönsson, B.; Khan, A. *J. Phys. Chem.* **1987**, *91*, 3291.

(21) Khan, A.; Marques, E. Catanionic surfactants. In *Specialist Surfactants*; Robb, I. D., Ed.; Blackie Academic & Professional: London, 1998; p 37.

(22) Tondre, C.; Caillet, C. *Adv. Colloid Interface Sci.* **2001**, *93*, 115.

(23) Li, X.; Ueda, K.; Kunieda, H. *Langmuir* **1999**, *15*, 7973.

(24) Li, X.; Kunieda, H. *Langmuir* **2000**, *16*, 10092.

(25) Li, X.; Kunieda, H. *Curr. Opin. Colloid Interface Sci.* **2003**, *8*, 327.

(26) Tieke, B. *Colloid Polym. Sci.* **2005**, *283*, 421.

(27) Abécassis, B.; Testard, F.; Arleth, L.; Hansen, S.; Grillo, I.; Zemb, T. *Langmuir* **2006**, *22*, 8017.

(28) Abécassis, B.; Testard, F.; Arleth, L.; Hansen, S.; Grillo, I.; Zemb, T. *Langmuir* **2007**, *23*, 9983.

(29) Hao, J. C.; Liu, W. M.; Xu, G. Y.; Zheng, L. Q. *Langmuir* **2003**, *19*, 10635.

(30) Hao, J. C.; Hoffmann, H. *Curr. Opin. Colloid Interface Sci.* **2004**, *9*, 279.

(31) Song, A.; Dong, S.; Jia, X.; Hao, J.; Liu, W.; Liu, T. *Angew. Chem., Int. Ed.* **2005**, *44*, 4018.

(32) Li, H.; Hao, J. *J. Phys. Chem. B* **2008**, *112*, 10497.

(33) Oda, R.; Narayanan, J.; Hassan, P. A.; Manohar, C.; Salkar, R. A.; Kern, F.; Candau, S. J. *Langmuir* **1998**, *14*, 4364.

(34) Coldren, B.; Warriner, H.; Van Zanten, R.; Zasadzinski, J. A.; Sirota, E. B. *Langmuir* **2006**, *22*, 2474.

(35) Silva, B. F. B.; Marques, E. F.; Olsson, U. *Langmuir* **2008**, *24*, 10746.

(36) Silva, B. F. B.; Marques, E. F.; Olsson, U. *J. Phys. Chem. B* **2007**, *111*, 13520.

(37) Arleth, L.; Pedersen, J. S. *Phys. Rev. E* **2001**, *63*, 061406.

(38) Balogh, J.; Olsson, U.; Pedersen, J. S. *J. Phys. Chem. B* **2007**, *111*, 682.

(39) *Neutrons, X-Rays and Light: Scattering Methods Applied to Soft Condensed Matter*, 1st ed.; Lindner, P., Zemb, T. Eds.; Elsevier Science B.V: Amsterdam, The Netherlands, 2002.

(40) Silva, B. F. B.; Marques, E. F. *J. Colloid Interface Sci.* **2005**, *290*, 267.

(41) Kohlbrecher, J.; Wagner, R. *J. Appl. Crystallogr.* **2000**, *33*, 804.

(42) Keiderling, U. *Appl. Phys. A* **2002**, *74*, S1455.

(43) Kohlbrecher, J. SASfit version 0.86; http://kur.web.psi.ch/sans1/ SANSSoft/sasfit.html.

(44) Pedersen, J. S. *Adv. Colloid Interface Sci.* **1997**, *70*, 171.

(45) D'Aguanno, B.; Klein, R. *J. Chem. Soc., Faraday Trans.* **1991**, *87*, 379.

(46) Evilevitch, A.; Lobaskin, V.; Olsson, U.; Linse, P.; Schurtenberger, P. *Langmuir* **2001**, *17*, 1043.

(47) Linse, P. OZ, version 4.0.1 ed.; Lund University; www.fkem1.lu.se/sm.

(48) Pedersen, J. S. *J. Phys. IV* **1993**, *3*, 491.

(49) Stilbs, P. *Prog. Nucl. Magn. Reson. Spectrosc.* **1987**, *19*, 1.

(50) Söderman, O.; Stilbs, P. *Prog. Nucl. Magn. Reson. Spectrosc.* **1994**, *26*, 445.

(51) Olsson, U.; Schurtenberger, P. *Langmuir* **1993**, *9*, 3389.

(52) Olsson, U.; Nakamura, K.; Kunieda, H.; Strey, R. *Langmuir* **1996**, *12*, 3045.

(53) Jönsson, B.; Jokela, P.; Khan, A.; Lindman, B.; Sadaghiani, A. *Langmuir* **1991**, *7*, 889.

(54) Scattering length density calculator; NIST; http://www.ncnr.nist.gov/ resources/sldcalc.html.

(55) Nägele, G.; Baur, P. *Physica A* **1997**, *245*, 297.

(56) Caponetti, E.; Floriano, M. A.; Didio, E.; Triolo, R. *J. Appl. Crystallogr.* **1993**, *26*, 612.

(57) Leaver, M.; Furó, I.; Olsson, U. *Langmuir* **1995**, *11*, 1524.

(58) Adamczyk, Z.; Bratek, A.; Jachimska, B.; Jasiński, T.; Warszyński, P. *J. Phys. Chem. B* **2006**, *110*, 22426.

(59) Linse, P. PB, version 2.2.5 ed.; Lund University; www.fkem1.lu.se/sm.

(60) Almgren, M.; Linse, P.; van der Auweraer, M.; Deschryver, F. C.; Geladé, E.; Croonen, Y. *J. Chem. Phys.* **1984**, *88*, 289.

(61) Engström, S.; Wennerström, H. *J. Phys. Chem.* **1978**, *82*, 2711.

(62) Wennerström, H. *Langmuir* **1990**, *6*, 834.

JP901752S